Complex 3D-Printed Mechanochromic Materials with Iridescent Structural Colors Based on Core–Shell Particles

Lukas Siegwardt and Markus Gallei*

A scalable protocol for design and subsequent 3D-printing of polymeric core-shell-particles is reported. The particle synthesis by emulsion polymerization in starved-feed mode is used for tailoring particle architecture and composition. Control of size, mechanical properties, and chemical functionalities allow to achieve the specific requirement profile for subsequent extrusion-based additive manufacturing. The core-shell particles consist of hard polystyrene cores and a comparably soft polyalkylacrylate-based shell. Size and monodispersity, as well as core-to-shell ratio, are determined by means of dynamic light scattering and transmission electron microscopy. Thermal and rheological properties are investigated by means of dynamic scanning calorimetry and thermogravimetric analysis as well as oscillation and capillary rheometry. During 3D-printing, the monodisperse particles self-assemble into an ordered close packed lattice structure, leading to visible reflection colors according to Bragg's law of diffraction. Distinct and angle-dependent reflection colors are recorded via UV-vis spectroscopy. As the structural color depends, inter alia, on the underlying particle sizes, resulting colors are easily tunable by adjusting the applied synthesis parameters. Under mechanical deformation, the color changes due to controlled lattice deformation, which enables mechanochromic sensing with the printed objects. They are also promising candidates for decorative ornaments, smart optical coatings, or advanced security devices.

1. Introduction

Within the last two decades, polymer-based core-shell-particles (CSP) have received increasing attention. In analogy to animals, like chameleons[1] or butterflies,[2] CSP-based materials reflect light, and in many cases these structures can respond to external triggers from the surrounding environment. Feasible stimuli comprise, for example, temperature, electric or magnetic fields, pH, solvents, and mechanical deformation.[3]

L. Siegwardt, M. Gallei
Saarland University
Polymer Chemistry
Campus C4 2, 66123 Saarbrücken, Germany
E-mail: markus.gallei@uni-saarland.de

The ORCID identification number(s) for the author(s) of this article can be found under https://doi.org/10.1002/adfm.202213099.

Application potentials range from anti-counterfeiting materials[4] and smart sensors[5] to optical coatings[6] and display technologies.[7]

Synthetic opals can be prepared using organic or inorganic materials and combinations thereof, featuring complex core particle and shell architectures. Elastomeric CSP can be prepared via stepwise starved-feed emulsion polymerization protocols.[3d,8] Often, these particles consist of a hard, crosslinked core surrounded by an immobilized soft shell. Diameters are tunable, usually ranging from 100 to 500 nm. During processing, the shell forms a continuous matrix around the dimensionally stable core particles. Elastomeric polymer opals can be fabricated to yield reversible stretch-tunable films, showing remarkable color changes due to mechanically induced deformation.[9]

Monodisperse CSP can self-assemble into long-range-ordered periodic lattices, so-called colloidal crystals. Due to periodical changes in the refractive index between core and shell, ordered CSP show Bragg-scattering, most importantly at the (111)-plane.[10] Such optical nanostructures are called photonic crystals. Macroscopic objects with underlying photonic crystal structures exhibit an iridescent structural color. Iridescence, otherwise known as goniochromism, describes the phenomenon of gradual color changes, depending on the angle of view or the angle of illumination. The reflected wavelength λ can be calculated with a modified version of the Bragg—Snell–Law, depicted in Equation 1. Reflected colors are influenced by the angle of incident light θ and the lattice constant a_{111}. The lattice constant is proportional to the particle diameter D. In addition, the mean effective refractive index n_{eff} of the CSP and the contrast in refractive indices between core and shell material influence intensity as well as color of reflected light, as described elsewhere.[10,11]

$$\lambda = 2a_{111}\sqrt{n_{eff}^2 - \cos^2\theta} = 2\sqrt{\frac{2}{3}}D\sqrt{n_{eff}^2 - \cos^2\theta} \qquad (1)$$

Several self-assembly strategies have been developed to produce ordered colloidal crystals from CSP, which has recently been reviewed by Li et al.[12] and other authors.[7b,9a,13] Many methods like drying,[14] spin coating,[15] or vertical deposition[13a] demand the presence of a substrate and a dispersion medium.

ADVANCED
SCIENCE NEWS
www.advancedsciencenews.com

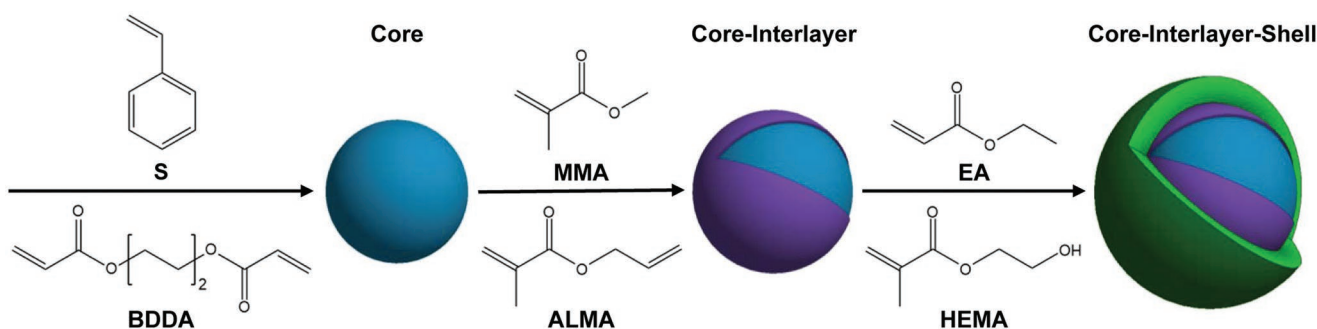ADVANCED
FUNCTIONAL
MATERIALS
www.afm-journal.de

Figure 1. Stepwise synthesis of CSP via starved-feed emulsion polymerization. The cores are comprised of S, cross-linked with BDDA. The subsequent polymerized interlayer consists of MMA and bifunctional ALMA as grafting anchor. For subsequent synthesis of the shell, EA and HEMA were used as monomers.

Compared to this, free-standing opal films are accessible via melt-shear organization technique.[8b,16] Using the bending induced oscillatory shearing (BIOS) process, elastomeric opal foils with lengths of several meters have been produced.[8a,17] Despite overcoming some disadvantages in producing stimuli-responsive structural colored materials, resulting polymeric opal films and foils are generally limited to 2D geometric shapes.[18] In the present work and for the first time, we used 3D-printing to process tailored CSP into complex 3D objects with iridescent stimuli-responsive structural color. Using the versatility of 3D-printing we aim to penetrate new markets and enhance the application possibilities of CSP.

Over the last decades, 3D-printing became an important method for local on-demand manufacturing. Adaptability and mass customization is highly sought after by industries such as healthcare[19] or sporting goods.[19a,20] 3D-printing produces complex shapes and lightweight structures, with increased sustainability, as nearly no raw material is wasted during processing. While primarily considered for R&D and prototyping purposes, 3D-printed parts are increasingly manufactured for end-use mechanical components and consumer goods in several industries, including automotive and aerospace,[19a,b,20] electronics,[19b,20] as well as construction.[19a,20]

3D-printing of smart polymers, which are responsive to several external triggers, has already been extensively reviewed[19c,d,21] and has for instance been investigated for wearable sensors,[19c,21b] optoelectronic devices,[19c,21a] soft robotics[19d,22] or self-healing materials.[21b,22] Within this context, one important feature of resulting materials is mechanochromism. Such materials change their color under mechanical deformation either on the molecular or macroscopic level. 3D-Printing of mechanochromic objects currently relies on the incorporation of inorganic mechanoluminescent materials[23] or organic mechanophores such as oxanorbornadiene[24] and spiropyran derivatives.[25]

A limiting factor for extrusion-based 3D-Printing of mechanoresponsive polymers is the lack in stability against high temperatures and shears of the mechanophores during processing.[21b] 3D-printing of particle-based materials exhibiting structural color would therefore pave the way to a new generation of stimuli-responsive materials and complex structures, overcoming this limitation. Beyond that, structural colors are advantageous to mechanoluminescent dies or pigments, as they exhibit more vivid color impressions, are environmentally friendly and do not fade or bleach over time.[26]

Structural colored materials have already been produced by direct-ink-writing[27] (DIW), fused-filament-fabrication[28] (FFF), and other 3D-printing technologies.[29] However, printed objects either lack in color diversity or 3D complexity, or do not possess smart features such as goniochromism or mechanochromism.

In this study, we present tailor-made CSP, which meet the prerequisites for extrusion-based 3D-printing. Specific defined rheological, thermal, and optical properties were achieved by starved-feed emulsion polymerization technique. The presented objects were printed on a DIW-FFF-hybrid printing system and combine iridescent mechanochromic structural color, as known from polymeric opal films, with a high level of detail, as known from commercial 3D-printing. By slightly adjusting synthesis parameters, the color of the final product was easily tunable. We envision our stimuli-responsive system as a promising candidate for the fabrication of smart optical sensors, anti-counterfeiting applications and other advanced optical devices.

2. Results and Discussion

2.1. Synthesis

Two batches, labelled CSP1 and CSP2, were prepared by semi-continuous and stepwise emulsion polymerization, as illustrated in **Figure 1**. Starved-feed mode for emulsion polymerization was necessary to synthesize monodisperse particles—a key feature for further processing and colloidal self-assembly. The synthesis of CSP and modifications for subsequent processing methods, for example, via melt-shear organization or BIOS, have been previously described.[3d,8a,b,9a] However, requirements to 3D-printable CSP differ with respect to thermal stability and rheology. Therefore, several aspects of the established synthesis had to be adjusted, including composition of the interlayer, selection of shell-monomers and core-to-shell ratio.

In the first step, poly(styrene-*co*-butanedioldiacrylate) (P(S-*co*-BDDA)) core-particles were synthesized. Two different core particle-batches C1 and C2 with different diameters were prepared by controlling the surfactant amount and monomer content during starved-feed mode. Compared to C1, we decreased the amount of surfactant in seed stage by 10% for C2 and increased the amount of monomer in starved-feed mode by 25%. As illustrated in **Figure 2**, the average diameters of the core particles were adjusted to be 175 and 222 nm, according
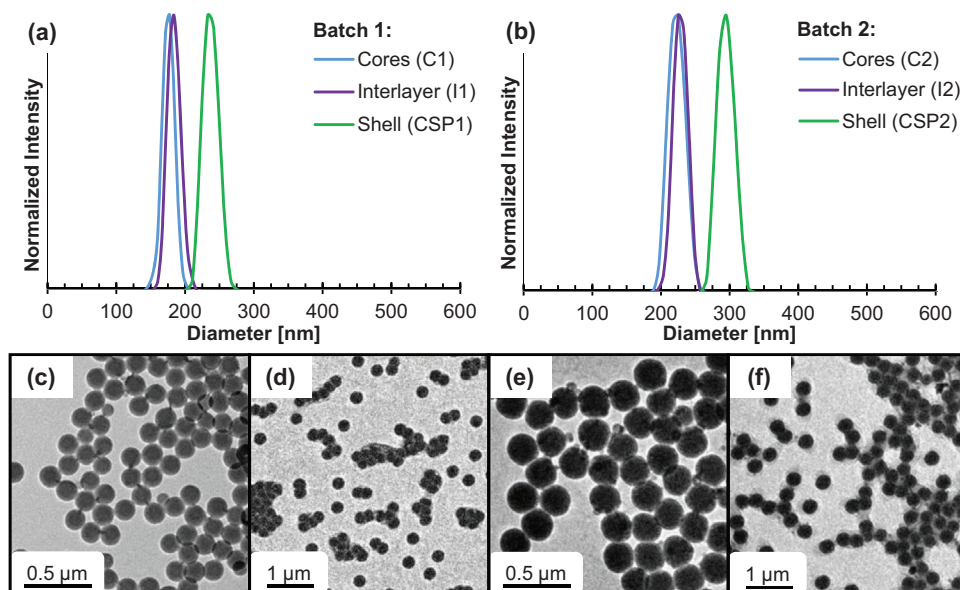
Figure 2. DLS measurements of a) CSP1 and b) CSP2 after each step of the emulsion polymerization. TEM images of c) the cores C1 and d) the final CSP1 as well as e) the cores C2 and f) the final CSP2.

to dynamic light scattering (DLS) measurements. Assuming a spherical geometry of the core particles, C2 shows roughly twice the volume of C1, which is in good accordance with literature[30] and expectations from the used recipe. The glass transition temperature of both core particle batches was determined to T_g(P(S-co-BDDA)) = 115°C by differential scanning calorimetry (DSC) measurements (Figure S1, Supporting Information). BDDA has been used as a crosslinking reagent to avoid deformation of the core particles upon processing. PS-particles crosslinked with BDDA are known to be dimensionally stable up to 190°C,[8c,31] and were therefore well suited for extrusion at 120°C and 3D-printing at 140°C.

In the second step, a crosslinked interlayer consisting of poly(methylmethacrylate-co-allylmethacrylate) (P(MMA-co-ALMA)) was introduced. Based on the two different reactive sites of ALMA, subsequent anchoring of a soft polymer shell material was possible.[9a] Covalent immobilization of the shell material was necessary to prevent detachment of polymer chains and, simultaneously, ensure stability of the CSP upon further processing. To achieve the desired covalent grafting, an ALMA-content of at least 5–10 wt% was required.[31] For the intended 3D-printing on the other hand, the content of ALMA had to be low enough to ensure that nearly all reactive moieties were consumed during grafting of the shell. Otherwise, separate particles tended to crosslink at elevated temperatures, resulting in an increase in viscosity during printing (Figure S2, Supporting Information). Increasing viscosity led to a loss of processability, as the material became brittle and non-extrudable. An ALMA-content of ≈ 6 wt% turned out to be a good balance, allowing sufficient grafting of the shell material for processing, but suppressing undesired crosslinking reactions during 3D-printing.

It is known from literature, that the exact core-to-shell ratio is crucial for film formation during the application of shear force driven organization techniques.[9a] If the volume fraction of soft shell polymer exceeds $\varphi_{Shell} > 60$ vol% (according to DLS measurements), some polymeric chains cannot be grafted to the interlayer. The presence of free ungrafted polymer chains impedes CSP assembly, resulting in a deterioration of structural color.[8a,31] Furthermore, CSP with a high shell content could not be printed with the herein used 3D-printing setup, due to the increased softness of the material. Higher soft shell amounts led to printed objects that could not keep their shape and tended to get wobbly, hindering deposition of subsequently printed layers. On the other hand, a reduction to $\varphi_{Shell} < 50$ vol% led to loss of processability, caused by crosslinking reactions of the CSP via non-consumed reactive moieties of the interlayer at elevated temperatures (Figure S2, Supporting Information). As a result, the material got brittle and could not be processed anymore. Moreover, CSP with low shell content showed flow instabilities during extrusion and were prone to melt fracture, due to their elevated viscosity. An optimized proportion of $\varphi_{Shell} = 53$–54 vol% turned out to be just low enough to facilitate self-assembly resulting in structurally colored materials, while being high enough to prevent subsequent crosslinking reactions and enabling a steady extrusion flow.

To produce 3D-printed objects featuring mechanochromic properties at room temperature, the resulting glass transition of the shell material had to be below room temperature. Furthermore, the effective refractive index contrast between core and shell had to be as high as possible to maximize color intensity.[7b,32] To meet these requirements, mainly ethyl acrylate (EA) was used as shell material. PEA features a low glass transition[33] of T_g(PEA) = −22°C and possess a relatively low refractive index[34] of n(PEA) = 1.47, compared to the core particles[34] with n(P(S-co-BDDA)) = 1.58.

Compared to this basic recipe, an additional 3 wt% of 2-hydroxyethylmethacrylate (HEMA) was incorporated into the shell material to improve mechanical properties. Upon HEMA incorporation, hardness, stiffness, and viscosity increased

Table 1. Comparison of the hydrodynamic diameters determined by DLS measurements of the diluted particle dispersions and corresponding TEM measurements of the particles in dried state. Volume fractions were calculated according to DLS measurements. Standard deviations are indicated with ±.

	Batch 1 Cores (C1)	Batch 1 Interlayer (I1)	Batch 1 Shell (CSP1)	Batch 2 Cores (C2)	Batch 2 Interlayer (I2)	Batch 2 Shell (CSP2)
D_{DLS} [nm]	175 ± 9	183 ± 10	237 ± 11	222 ± 12	228 ± 10	294 ± 12
φ [vol%]	40.6%	6.0%	53.4%	43.3%	3.2%	53.5%
D_{TEM} [nm]	148 ± 6	/	211 ± 10	178 ± 6	/	249 ± 8
T_g [°C]	115	/	−7	115	/	−9

at room temperature (Table S1, Supporting Information). Therefore, the mechanical stability and dimensional accuracy of 3D-printed parts increased. We attribute this reinforcement to the elevated glass transition of $T_g(P(EA\text{-}co\text{-}HEMA))$ ≈ -8°C (Figure S1, Supporting Information) and to the introduction of hydrogen bonds, due to hydroxyl moieties in HEMA.

Another beneficial effect upon incorporation of HEMA was the increased shear-thinning, confirmed by rheological measurements (Figure S3 and Table S2, Supporting Information). Shear-thinning improves the suitability for extrusion based 3D-printing, enabling flowing and extruding under high shear and immediate shape retention postdeposition.[22] Again, we attribute this observation to the introduction of hydrogen bonds, which is a literature-known shear-thinning mechanism in PHEMA-containing materials. The use of non-covalent bonds, especially hydrogen bonds, is a frequently used strategy to construct polymeric materials with improved processability via 3D-printing.[21b,22,27a] During printing, the physical bonds are easily broken upon mechanical shearing. The multivalent interactions are disrupted, producing a low viscosity liquid. After extrusion, when the shear force is removed, viscosity increases sharply due to the rapid association of hydrogen bonds into a highly mobile and transient non-covalent network, wherein physical crosslinks are re-established.

The successful preparation of tailormade CSP through the applied synthetic protocol was verified by DLS measurements of the diluted particle dispersions, shown in Figure 2. As listed in **Table 1**, the hydrodynamic diameter D_{DLS} increased after each step of the semi-continuous emulsion polymerization. As the same protocol for shell- and interlayer-synthesis was applied for both batches, similar core-to-shell ratios were obtained.

To further evaluate the successful preparation of CSP and to determine the particle diameter in dried state D_{TEM}, transmission electron microscope (TEM) measurements were carried out (Figure 2). From these images can be concluded that well-defined cores and CSP were prepared. Corresponding diameters are listed in Table 1. Given the different diameters of the two batches, different reflection colors for the intended 3D-printed objects were expected, according to Equation 1.

The difference between particle sizes determined by DLS and TEM investigations is related to intrinsic differences between the methods. DLS experiments determine the hydrodynamic diameter. Particles are examined in a swollen state, depending on interactions with the respective solvent or dispersion medium. Diameters in the dried state, determined by TEM measurements, were therefore found to be considerably smaller. All data on particle sizes is in good agreement with expectations, particularly regarding the monomer consumption

and core-to-shell ratio. The low relative standard deviations of $\sigma_{DLS} < 6\%$ and $\sigma_{TEM} < 5\%$, confirmed the excellent control over the polymerization, leading to monodisperse particles.

2.2. Processing

An overview of the processing steps is provided in **Figure 3**. After synthesis, the lyophilized particle mass was mixed with 0.03 wt% carbon black. Carbon black is known to improve structural color, by absorbing diffuse scattered light.[36] The incorporation of carbon black presumably influenced the self-assembly and introduced lattice defects. However, due to the very low concentration, defects should be locally restricted and overall scarce, hence not influencing macroscopic properties of 3D-printed objects. Pursiainen et al.[37] already proved that carbon doping at such low concentrations does not affect the microstructure of opaline films prepared via melt-shearing. Given the similarity of therein used and herein presented CSP, as well as the similar driving force for self-assembly (shearing at elevated temperatures), we assume that the findings of Pursiainen et al. are mostly transferable to the herein investigated system.

Prior to 3D-printing, the mixture of CSP and carbon black was homogenized and densified in a microextruder at 120°C. The used Saarpricom Delta UpSD 3D-Printer is mostly set up like a common Delta-FFF-printer. In contrast to most commercial printers, the extrusion-head is fixed in position, while the printing bed moves in X,Y and Z-direction. The extrusion head is equipped with a piston extruder, similar to common DIW-printers. The extruded strand was granulated and filled into the cylinder of this piston extruder. During 3D-printing, the CSP were extruded through the nozzle of the printer, driven by the piston pushing the granulated mass downward. Close-up pictures of the printing system are provided in Figure S4 (Supporting Information). We used a PET-coated printing bed, which provided a good balance between sufficient adhesion during printing and effortless removal afterward.

Selected printing parameters are depicted in **Table 2**, while an extensive overview of slicing parameters is provided in Table S3 (Supporting Information). As the model is built layer by layer, the layer thickness of 0.18 mm dictates the final resolution in vertical direction. The layer width of 0.50 mm determines the resolution in horizontal direction. Supports were disabled by default during printing and no further processing, finishing or removal of residues was applied.

To successfully print the extruded mass consisting of CSP and carbon black, the printing temperature T_P was of utmost
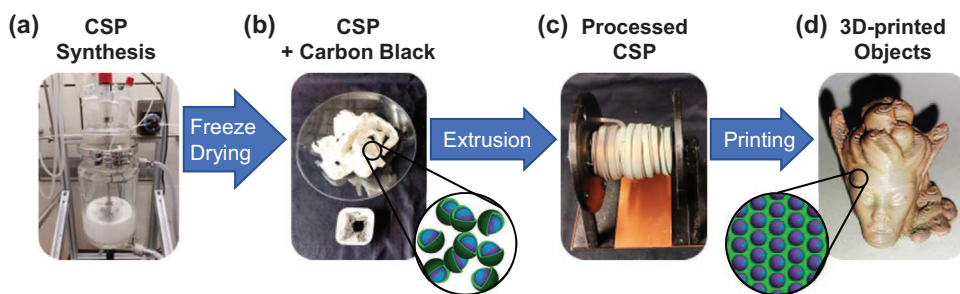
Figure 3. a) Starting from polymer synthesis via starved-feed emulsion-polymerization, b) the CSP were freeze-dried and mixed with carbon black. The lyophilized polymer was composed of disordered CSP (magnified scheme), showing no structural color. c) Using a microextruder, the mixture was homogenized and densified. The herein shown extruded strand was reeled up on a spool. d) The extruded strand was granulated, filled into the piston extruder of the printer and 3D-printed. During extrusion and subsequent 3D-printing, the CSP were exhibited to high shear forces and self-assembled into an ordered colloidal crystalline structure (magnified scheme), resulting in iridescent structural color. The extruded mixture and the 3D-printed elf (height: 21 mm, 3D-model remixed and reproduced under terms of the CC-BY 4.0 license.[35] Copyright 2018, M. Dost) are composed of CSP2.

importance. Temperature dependent viscosity behavior of CSP has been previously investigated by Finlayson and Baumberg.[38] In accordance with literature, we observed a decrease in complex viscosity by approximately one order of magnitude in heating from room temperature up to 100°C, as depicted in **Figure 4**a. The small viscosity-drop at 120°C is related to the glass transition of the core particles but appears almost negligible. Due to the high degree of crosslinking sites, the cores' thermomechanical properties resemble mostly the behavior of a thermoset, rather than a thermoplastic polymer. Overall, viscosity rapidly decreases upon heating from room temperature and then flattens off asymptotically, which resembles the common behavior of an elastomer with non-covalent physical crosslinking sites. We therefore conclude that the thermomechanical properties of the CSP are mainly influenced and controllable by composition and amount of the elastomeric shell material, confirming experimentally the findings of Finlayson and Baumberg.[38]

In order to enable the piston to extrude polymer through the nozzle, the printing temperature had to be high enough to sufficiently lower viscosity. At $T_P \approx 120$°C, the workload of the piston extruder approached its maximum capacity of 100%. Thus, we determined a lower limit of $T_P \geq 130$°C. As depicted in Figure 4a, this was caused by an increase in viscosity, as temperature-dependence of the complex viscosity and workload correlate qualitatively. Differences in curve progression arise from differences in the measurement-modi, as described in detail in Annotation S1 (Supporting Information).

To determine an upper temperature limit, we investigated thermal degradation properties of the dried CSP. According to thermogravimetric analysis (TGA), degradation started at 224 and 230°C, for CSP1 and CSP2, respectively (Figure S5, Supporting Information). We further identified oxidation induction temperatures by using DSC measurements of 194 and 196°C, for CSP1 and CSP2, respectively (Figure S6, Supporting Information). Therefore, printing at $T_P > 180$°C was avoided. In general, higher temperatures are beneficial for layer adhesion and decrease the risk of a clogged nozzle.[22,39] Lower temperatures on the other hand reduce stringing and especially warping, which proved to be a major limiting factor for printing quality. Given all these considerations we set $T_P = 140$°C as default printing temperature.

As depicted in Figure 4b, the extruded mass turned out to be highly shear-thinning. It is known from literature, that the grafted soft shell polymer forms a quasi-continuous viscoelastic matrix around the rigid cores. Without external shear forces, mobility of the rigid spheres is highly inhibited by the gum-like matrix and Brownian motion is suppressed.[8a,38,40] Given these prerequisites, we assume that the following mechanisms contribute to the observed shear-thinning: Shear-induced disentanglements of polymer strands of the grafted shell polymer decrease the flow resistance of individual particles. The generation of non-equilibrium structures, such as strings, may also decrease flow resistance under shear force. Additionally, shearing enables sliding of particle layers and the formation of flowmechanically favorable particle orientations. All these shear-thinning mechanisms are further amplified by the introduction of hydrogen-bonds, due to HEMA-incorporation in the shell material, which has already been discussed in the previous chapter.

Shear-thinning behavior is beneficial for extrusion-based additive manufacturing and enables high printing speeds.[22,27a] We chose a default printing speed of 400 mm min⁻¹ to keep the workload of the piston extruder at moderate levels of 50–70%. Given this printing speed, we calculated shear rates inside the

Table 2. Overview of selected printing parameters and calculations of shear rates during the printing process.

Parameter	Description	Value
Temperature T_P	Print Setting	140°C
Infill Percentage	Print Setting	30%
Printing Speed v	Print Setting	400 mm min⁻¹
Extrusion width w	Print Setting	0.50 mm
Layer Height h	Print Setting	0.18 mm
Flow rate $\dot{V}$	$\dot{V} = v \cdot w \cdot h$	0.60 mm³ s⁻¹
Nozzle Diameter d	Machine Parameter	0.40 mm
Shear rate nozzle $\dot{\gamma}_{Nozzle}$	$\dot{\gamma}_{Nozzle} = \dfrac{\dot{V}}{0.25\pi\, d^2 \cdot 0.5\, d}$	23.9 s⁻¹
Shear rate print $\dot{\gamma}_{Print}$	$\dot{\gamma}_{Print} = \dfrac{v}{h}$	37.0 s⁻¹

**ADVANCED
SCIENCE NEWS**

www.advancedsciencenews.com

**ADVANCED
FUNCTIONAL
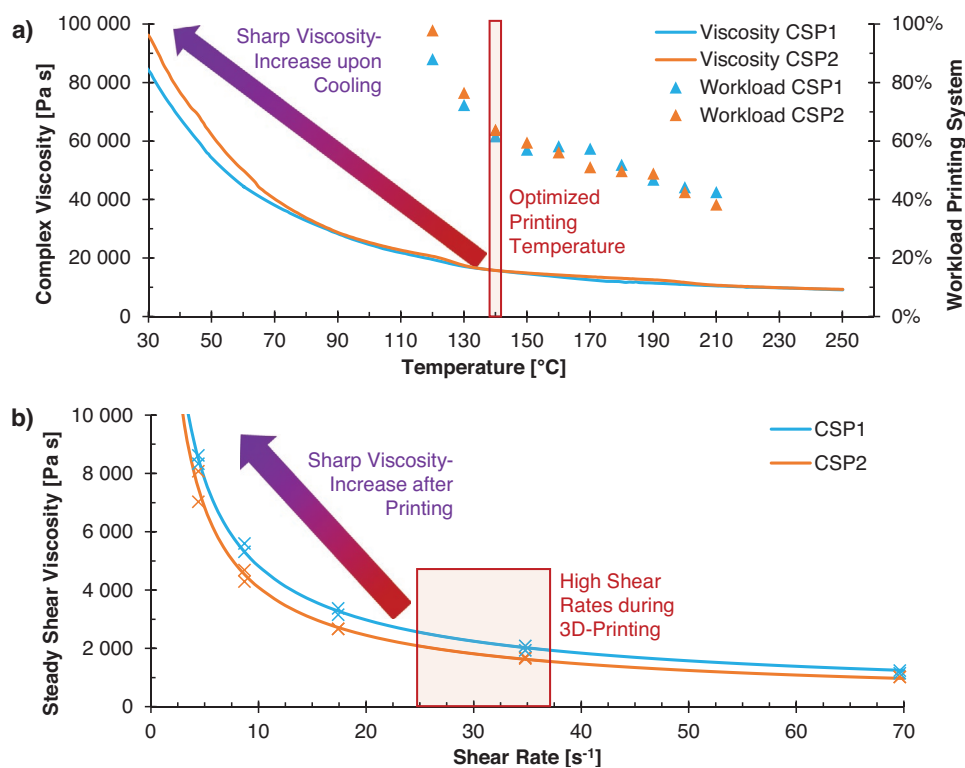MATERIALS**

www.afm-journal.de

Figure 4. Rheological examination of the thermomechanical properties in terms of dynamic viscosities of the synthesized CSP. During printing (indicated with a red rectangle), the particles were exposed to an elevated temperature and high shear forces. After printing, the object was cooled down and not exposed to shear forces anymore, resulting in a sharp viscosity-increase. a) Temperature-Sweep. Complex viscosities (solid lines) were determined in oscillation within the linear-viscoelastic regime. 299 measurement points were connected using polynomial smoothed lines. Workloads (triangular points) of the printing system were read off during 3D-printing from a load cell, integrated in the piston extruder of the printer. A workload of 100% represents the highest possible extrusion force. b) Frequency-Sweep. The steady shear viscosity was determined in a slit-capillary rheometer. Measured steady shear viscosities are indicated with a cross. Measurement points were connected and interpolated by fitting Ostwald-de-Waele Power Laws. Details on the Power–Law fit are provided in the Figure S3 (Supporting Information).

cross-section of the nozzle to be $\dot{\gamma}_{Nozzle} = 23.9$ s^{-1} and between moving bed and stationary tip of the nozzle during printing to be $\dot{\gamma}_{Print} = 37.0$ s^{-1}. Calculations are provided in Table 2 and further discussed in Annotation S2 (Supporting Information).

In summary, tuning of temperature- and shear-dependent flow behavior via adjustments of polymer synthesis enabled successful 3D-printing. During printing, the material could be extruded easily, owing to the reduced viscosity under shear force and elevated temperature. Once printed, the material was not exposed to shear forces anymore and cooled down to room temperature. Therefore, viscosity increased rapidly, providing dimensional accuracy and a stable foundation for following layers. With these prerequisites, we were able to print structural colored objects with unseen 3D complexity. Moreover, our method proved to be applicable to produce 2D structures like logos or signs, as well as tensile test specimen, without the need for a mask or post processing.

2.3. Optical Properties and Structural Color

3D-printed objects revealed vivid structural colors due to Bragg diffraction at the underlying colloidal crystal structure. As shown in Figure 3c, the extruded mass already showed

faint structural color, indicating a shear-driven self-assembly of the CSP during extrusion. While we cannot rule out, that local domains kept thereby established near order during subsequent 3D-printing, we assume that the ordering during extrusion did not affect the final order in 3D-printed objects. During 3D-printing, particle mobility was increased due to shear-thinning and elevated temperature (Figure 4), while the CSP were exhibited to high shear rates and extruded with high flow velocities (Table 2). These conditions presumably led to an independent self-assembly into the final ordered structures during 3D-printing, which will be discussed in the following.

To demonstrate the combination of convenient synthesis and resulting color appearance, two different batches of CSP were synthesized. Due to differences in particle size, CSP1 and CSP2 displayed different colors within 3D-printed objects. Both batches share the same composition and almost similar core-interlayer-shell-proportion. Therefore, both possess the same effective refractive index of $n_{eff} = 1.52$. The effective refractive index was calculated from the refractive indices of the pure polymers[34] [n(PS) = 1.59; n(PBDDA) = 1.46; n(PMMA) = 1.48; n(PALMA) = 1.52; n(PEA) = 1.47; n(PHEMA) = 1.51] and their volume fractions in the resulting CSP, according to DLS data (Table 1).
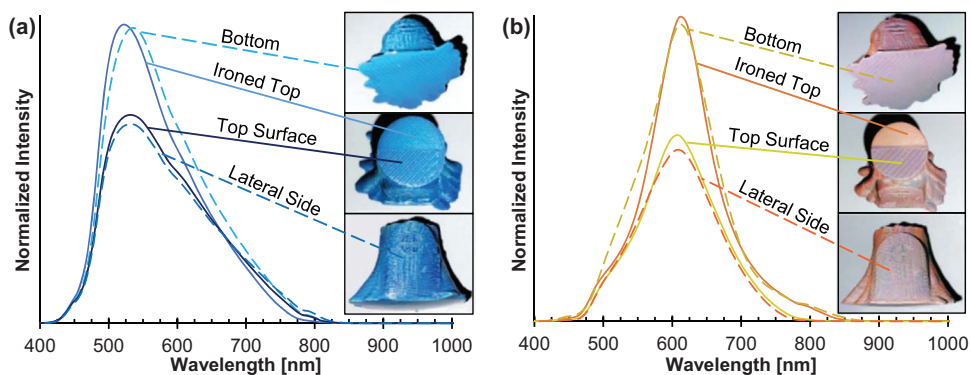
Figure 5. Reflection spectra at different positions of printed objects. 73 measurement points per each spectrum were connected using polynomial smoothed lines. Inserted pictures show a small house (height: 19 mm) in shape of a tree (for gnomes, goblins, and other forest dwellers) from different directions to assign spectra to the respective position of measurement. All spectra were measured under normal incidence. Pictures were taken without background lighting and activated camera flashlight to mimic normal light incidence. The rear halves of the top surfaces were refined with an ironing-script. a) Measurements on specimen composed of the smaller CSP1, appearing turquoise. b) Measurements on specimen composed of the bigger CSP2, appearing orange.

Reflection spectra of 3D-printed objects composed of CSP1 and CSP2 were recorded on different surfaces of the prints (**Figure 5**). Peak positions were found to be independent on the printed surface. As listed in **Table 3**, all measured peak wavelengths are in good agreement with the expected λ(Bragg) according to Equation 1. The small standard deviation of $\sigma_\lambda = 10$ nm implies that the particles self-assembled during printing into colloidal crystalline structures, as known from established shear-driven methods like melt-shear organization[8b,16] or the BIOS process.[8a,17]

According to Figure 5, color intensities at the bottom of printed objects were found to be considerably higher, compared to lateral surfaces or the top surface. At the flat bottom surface, the crystalline structure was highly perpendicular to the incoming light at normal incidence, resulting in a narrow and intense reflection peak. The lateral side and top surface are furrowed, due to imperfect merging of single layers and lines. Incoming light hit those surfaces under a variety of incident angles, which presumably resulted in the observed broadening of the peak. Furthermore, reflection angles at the side and top surfaces also deviated from normal reflection, due to the furrowed structure. Therefore, less rays of light hit the reflection detector in normal position, resulting in a decreased peak intensity.

Presumably, different shear forces further enhanced the divergence in color intensity on different surfaces. It is

known from literature, that higher shear forces lead to better self-assembly and a higher degree of order in the crystalline structure, resulting in more intense structural color.[8a,38a,40,41] In contrast to already printed parts, the printing bed provided a rigid and non-deformable surface. Therefore, shear forces between nozzle and bed (representing the bottom of the first layer) were higher and colors were found to be more intense. Shear forces between nozzle and partly printed parts (representing the top surface and the lateral sides of the objects) were lower, owing to the softness and deformability of the printed material, due to its elastomeric character.

With the implementation of an ironing-script, we were able to improve the color intensity on top surfaces. Ironing was achieved by moving the nozzle back and forth over the top layer. It grinded any material sticking up down into the top of the print by pushing the nozzle over it. Detailed ironing-settings are listed in Table S4 (Supporting Information). We attribute the increase in intensity to the resulting flatter surface and additional shearing forces during ironing.

Scanning electron microscope (SEM) images of the top printed surface (**Figure 6**) further prove successful self-assembly of the CSP in 3D-printed objects. Particles were partially assembled into hexagonally arranged structures, which is typical for a face-centered-cubic packing structure. Colloidal near order can best be described as random closed packed and resembles order in natural and artificial opals. While a perfect long-range order is not observable, the degree of order is nevertheless high enough to show optically visible structural color and narrow reflection peaks. Distinct angle-dependence and strain-dependence of the structural color will be demonstrated in the following chapter, further proving that there must be at least partial long-range order.

In analogy to the investigations of different printing surfaces, we further examined the influence of different printing directions on structural color (Figure S7, Supporting Information). We compared rectilinear and concentric infill patterns. Once again, measured peak wavelengths were found to be independent on the printing direction. We assume, that this observation is caused by the isotropic and symmetrical

Table 3. Expected and measured peak wavelengths at different surfaces of printed objects. Expected peak wavelengths λ(Bragg) were calculated according to Equation 1, using particle diameters in dried state. Measured peak wavelengths λ(print surface) were recorded under normal light incidence.

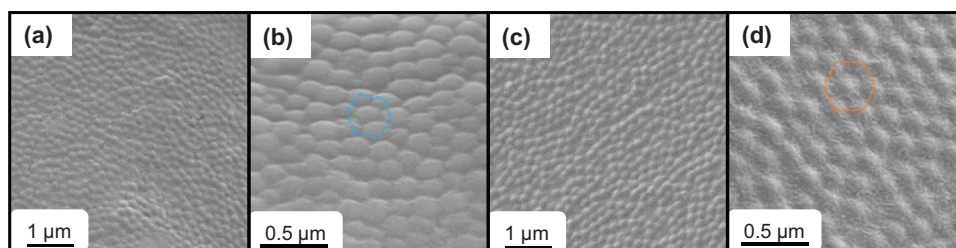|	CSP1	CSP2
λ(Bragg) [nm]	523	618
λ(Bottom) [nm]	533	616
λ(Lateral Side) [nm]	532	609
λ(Top Surface) [nm]	536	602
λ(Ironed Top) [nm]	526	609

Figure 6. SEM images in two different magnifications of the top surface of a 3D-printed specimen, composed of a,b) CSP1 and c,d) CSP2.

nature of the closed packed lattice. As described by Phillips et al., anisotropic structures would lead to a shift of the reflected wavelength.[42] However, as peak positions were found to be independent on the printed geometry (Table 3; Table S5, Supporting Information) and no lattice-distortion or preferred direction is observable within the corresponding SEM images (Figure 6), we conclude that different printing paths do not have an impact on the established lattice structure.

2.4. Stimuli-Responsiveness: Angle-Dependency and Mechanochromism

As expected from Equation 1, the color of the printed objects was found to be dependent on the angle of view. **Figure 7** shows angle-dependent UV–vis reflection measurements on the bottom surface of a 3D-printed test specimen in shape of a butterfly. Imprinted on the butterfly are the letters "UdS" for "Universität des Saarlandes" (Saarland University). Analogous measurements were performed on test specimen composed of CSP1 and CSP2. The prepared samples show angle-dependent reflection colors in a range from 90° to 30°. Under normal light incidence turquoise (CSP1) and orange (CSP2) reflection colors were measured, respectively. With increasingly steeper angles, the reflection colors blue shifted to shorter wavelengths. Inserted pictures demonstrate a visible color change from turquoise to blue-violet (CSP1) and orange to green (CSP2), respectively.

Following Equation 1, we calculated the expected peak wavelengths under different angles according to TEM-diameters.
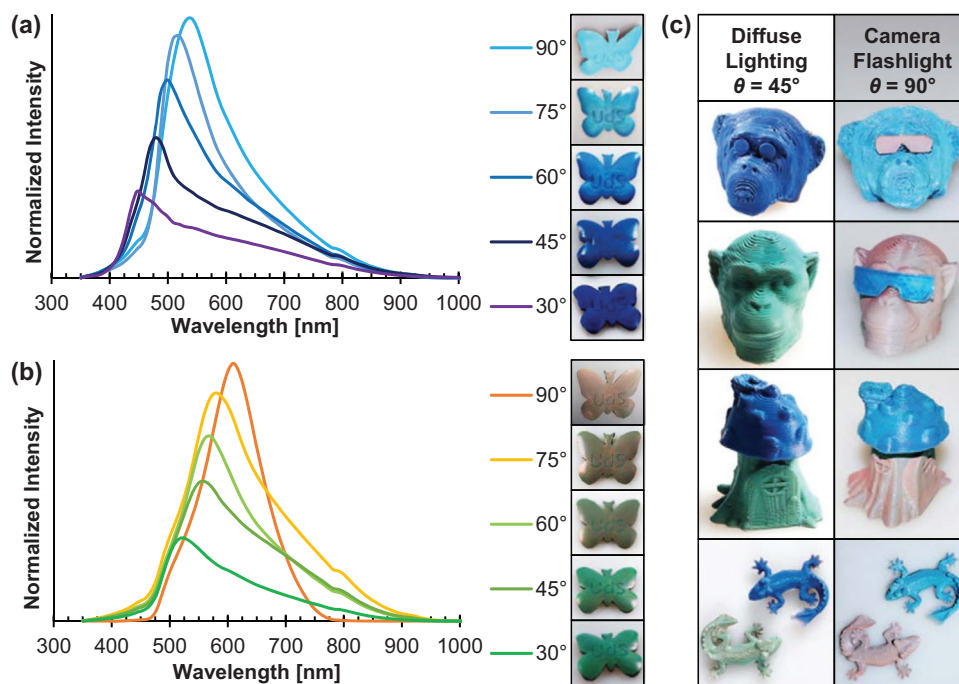

Figure 7. Angle dependent optical reflection spectra and referring photographs of the bottom surface of a 3D-printed butterfly (width: 35 mm) composed of a) CSP1 and b) CSP2. An angle of 90° refers to normal incidence and normal reflection. 73 measurement points per each measurement were connected using polynomial smoothed lines. Pictures were taken after measurement without background lighting and activated camera flashlight to mimic normal light-incidence. c) Photographs of a gorilla (top row, height: 25 mm, eyes refined with an ironing-script, 3D-model remixed and reproduced under terms of the CC-BY 4.0 license.[43] Copyright 2018, S. Campbell), a chimpanzee (second row, height: 17 mm, 3D-model remixed and reproduced under terms of the CC-BY 4.0 license.[44] Copyright 2018, S. Campbell), a tree house with roof (third row, height: 35 mm) and two geckos (bottom row, length: 45 mm) composed of CSP1 (blue-turquoise objects) and CSP2 (green-orange objects). Pictures in the left column were taken under diffuse lighting, leading to reflections at every incidence angle from 0 to 90°, on average 45°. Pictures in the right column were taken without background lighting and activated camera flashlight, leading to reflections at an incidence angle of mostly 90°. No animals were harmed, as the apes are protected from the flashlight with 3D-printed sunglasses.

2213099 (8 of 13)

Table 4. Expected and measured peak wavelengths under different angles. Expected λ(Bragg) were calculated according to Equation 1. Particle diameters in dried state, according to TEM-experiments, were used for all calculations.

Angle θ	CSP1 λ(Bragg) [nm]	CSP1 λ(Measured) [nm]	CSP2 λ(Bragg) [nm]	CSP2 λ(Measured) [nm]
90°	524	539	618	611
75°	516	514	609	583
60°	495	498	584	565
45°	464	479	547	558
30°	430	449	508	518

As listed in **Table 4**, measured peaks are in good agreement with expectations, indicated by the small standard deviation of $\sigma_\lambda = 15$ nm. These results further prove that the iridescent structural color is a result of highly ordered close packed particle domains and that the colloidal crystal structure must possess long-range order.

Photographs in Figure 7c show how the color of complex printed objects changes under different lighting conditions. Without background lighting and activated flashlight, objects appear turquoise (CSP1) and orange (CSP2), depending on which particles where processed. This photography mode is equivalent to normal light incidence at $\theta = 90°$. Diffuse lighting on the other hand resembles light incidence at every possible angle from 0–90°, resulting in an average angle of $\overline{\theta} = 45°$. Under diffuse lighting, the color of the objects changes from turquoise to blue (CSP1) and orange to green (CSP2), respectively. This visually observed goniochromism is in good accordance with the angle-dependent reflection measurements.

Besides the angle of incident light, the reflected color should depend on the lattice constant and therefore be responsible to mechanical deformation. Since the printed CSP feature an elastomeric shell, objects could be drawn at room temperature, accompanied by an observable color change upon stretching. To investigate the mechanochromic properties, reflection spectra at different strains ε under normal light incidence were recorded (**Figure 8**). Tests were performed on the ironed top surfaces of 3D-printed tensile test specimens in shape of dog bones. Dimensions of the test specimens are sketched in Figure S8 (Supporting Information).

The mechanochromic properties of CSP have been subject of extensive research.[36,45] It is therefore well known that the distance between individual CSP horizontal to the stretching direction increases under strain, resulting in a decrease in the lattice constant along the vertical direction. According to Equation 1, a decreasing lattice constant should lead to a visible blue shift of reflection color—such a shift was indeed observed, as shown in Figure 8. We also recorded spectra of compressed dog bones at $\varepsilon = -10\%$, showing a red shift of the peak. Both batches of CSP displayed peak wavelength shifts of more than 100 nm due to mechanical deformation.

Different approaches have been proposed to predict the color change under strain. Ruhl et al.[45b] proposed a simple strain dependency of the reflected wavelength $\lambda(\varepsilon)$ following geometrical considerations, as listed in Equation 2:

$$\lambda(\varepsilon) = \frac{\lambda(0\%)}{1 + 0.5\varepsilon} \tag{2}$$

Viel et al.[45c] included the Poisson's ratio v, as depicted in Equation 3:

$$\lambda(\varepsilon) = \lambda(0\%) \cdot (1 - v\varepsilon) = \lambda(0\%) \cdot (1 - 0.5\varepsilon) \tag{3}$$

Following Equations 2 and 3, we calculated the expected shifts according to both models in **Table 5**. We experimentally determined Poisson's ratios of $v = 0.41$ for CSP1 and $v = 0.44$ for CSP2, as calculated and discussed below (**Table 6**). The expected peaks without strain $\lambda(0\%)$ were calculated according to Equation 1 and TEM-diameters. In the scope of this study none of the used models proved superior to the other one. Both models are in good agreement with measured values, resulting in similar standard deviations of σ_λ(Ruhl) = 7 and σ_λ(Viel) = 7 nm. Once again, these results prove that the intense structural color is a result of highly ordered colloidal crystal structures inside the printed object and the presence of long-range ordered domains.

As observable in the photographs in Figure 8, the mechanochromic response is not limited to tensile strain. Other types of mechanical deformation, like compression, bending, torsion, or indentation also led to visible color changes, making the material suitable for a broad range of sensing applications. During mechanical deformation, a decrease in reflection intensity was observable, due to a loss of colloidal crystalline order upon lattice deformation. However, when the test specimens were allowed to relax to their original state, the embedded PS cores reassembled with nearly identical lattice spacing, as the original color was fully recovered.

2.5. Mechanical Properties

Mechanical properties are important for mechanochromic sensing applications. We therefore conducted tensile tests on 3D-printed test specimen to determine the tensile modulus E and the yield point. Corresponding stress strain diagrams are presented in Figure S9 (Supporting Information). We further determined the shear modulus G with oscillatory rheometry and the Shore-A hardness of both batches. The Poisson's ratio v was calculated according to Equation 4, assuming isotropic material properties.

$$v = \frac{E}{2G} - 1 \tag{4}$$

The examined mechanical properties are summarized in Table 6. As discussed above (chapter 2.2 Processing),
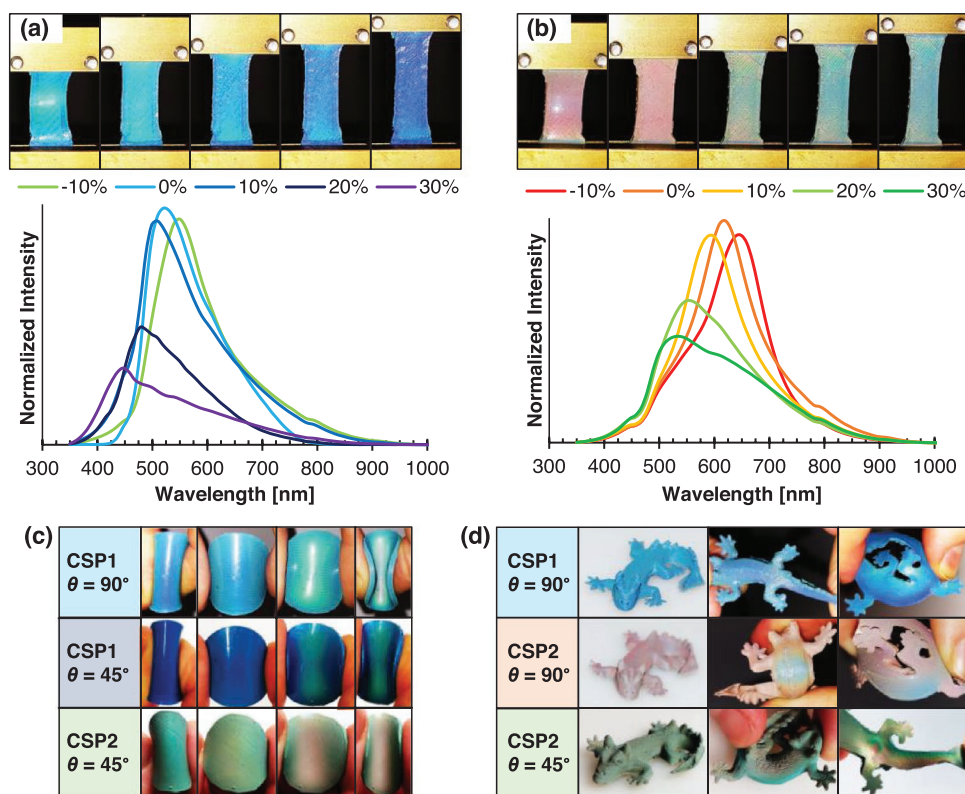
Figure 8. a,b) Normal-incidence optical reflection spectra of 3D-printed tensile test specimen (initial length: 25 mm) under different strains. 73 measurement points per each measurement were connected using polynomial smoothed lines. During measurement, the test-specimen were fixated in a test clamp. Pictures were taken without background lighting and activated camera flashlight to mimic normal light-incidence. Analogous measurements were performed for (a) CSP1 and (b) CSP2. c,d) Photographs of 3D-printed (c) Slices (diameter: 30 mm, thickness: 2 mm) and (d) Geckos, composed of CSP1 and CSP2, under different lighting conditions in several manually applied bending states.

thermo-rheological properties of the CSP are mainly dictated by the soft shell material. Given the low moduli, as well as the low hardness, this conclusion is further verified for mechanical properties at room temperature. The obtained Poisson's ratios also fall in the typical range of a soft polymer.[46] As particles in printed objects are not covalently crosslinked, the response to mechanical deformation is partly viscous. However, it is known from literature, that strains below the yield point lead to an almost fully elastic response of the CSP. Entanglements of polymeric chains in the particle shell act as physical crosslinkers between particles.[45a,c] With the herein determined yield strains of roughly 40%, we were able to prove the applicability of this literature-known mechanism to our system. All examined

strains that were used to trigger mechanochromic responses are well below the yield point and can therefore be considered reversible.

In summary, the thermomechanical properties of the herein presented CSP resemble the behavior of a non-covalent crosslinked thermoplastic elastomer, which makes them well suited for a broad range of sensing applications. The absolute mechanical properties are easily tailorable to the specific application, for instance by varying object thickness, number of outlines, or infill ratio—a decisive advantage of 3D-printing, compared to state-of-the-art processing methods. Reversibility and visibility of the mechanochromic response over 25 cycles is further demonstrated in Video S1 (Supporting Information).

Table 5. Expected and measured peak wavelengths at different strains under normal incidence. Expected λ(Ruhl) were calculated with Equation 2. Expected λ(Viel) were calculated with Equation 3. Particle diameters in dried state, according to TEM-experiments, were used for all calculations. The negative strain refers to a measurement in compression.

Strain ε	CSP1 λ(Ruhl) [nm]	CSP1 λ(Viel) [nm]	CSP1 λ(Measured) [nm]	CSP2 λ(Ruhl) [nm]	CSP2 λ(Viel) [nm]	CSP2 λ(Measured) [nm]
−10%	551	545	550	651	645	641
0%	524	524	526	618	618	615
10%	499	502	506	589	591	591
20%	476	481	479	562	564	550
30%	455	459	447	537	536	530

Table 6. Mechanical properties at room temperature. Yield strains and tensile moduli were determined via tensile testing. Shear moduli were determined using oscillation rheometry.

Material Property	CSP1	CSP2
Shore-A Hardness	75	71
Yield Strain	43%	39%
Tensile Modulus [MPa]	1.72	1.78
Shear Modulus [MPa]	0.61	0.62
Poisson's Ratio	0.41	0.44

3. Conclusion

In summary, we presented the synthesis and processing of the first 3D-printed CSP, showing goniochromic and mechanochromic structural color. TEM, DLS, and DSC measurements proved the success of every synthetic step of the applied semicontinuous emulsion polymerization protocol. After freeze drying, extrusion and 3D-printing of the CSP, highly detailed objects were obtained. 3D-prints produced in such a highly controlled manner combine unseen geometrical complexity with iridescent, stimuli-responsive structural color. As demonstrated, colors are easily tunable by controlling the particle size during synthesis. Fascinating optical properties and mechanically triggered wavelength-shifts of more than 100 nm were shown by UV–vis spectroscopy and photographs.

We envision herein presented methods to open new avenues for a variety of applications for CSP. In the field of deformation sensing, established processing methods were limited to round or rectangular 2D-structures with restricted variability of film-thickness.[8a,b,9a,16b,17,47] Using our 3D-printing-based approach, the geometry of the sensor is effortlessly tailorable to the specific problem, while mechanical properties are adjustable. For anti-counterfeiting materials or optical display technologies, state-of-the-art methods rely on the use of a mask and post-processing for the implementation of logos, signs or text. 3D-printing not only removes this time- and resource consuming steps, but also offers a broad freedom of design and the possibility of mass customization.

4. Experimental Section

Materials: Styrene (S, 99%) was purchased from Fisher Scientific. Butanedioldiacrylate (BDDA, 90%), methylmethacrylate (MMA, 99%), ethylacrylate (EA, 99.5%), and 2-hydroxyethylmethacrylate (HEMA, 97%) were purchased from Sigma–Aldrich. Allylmethacrylate (ALMA, 98%) was purchased from TCI. Prior to emulsion polymerization, radical inhibitors were removed from the monomers by passing them through a basic alumina column (50–200 µm, Acros Organics). Potassium hydroxide flakes (KOH, 90% reagent grade), sodium disulfite (NaDS for analysis), sodium persulfate (NaPS, ≥ 98%), and sodium dodecyl sulfate (SDS, ≥ 98.5%) were purchased from Sigma-Aldrich. Dowfax2A1 was obtained from Dow Chemicals.

Core-Synthesis: Two Batches of crosslinked polystyrene core particles were synthesized in a 5 L double-wall reactor, equipped with a reflux condenser and a stirrer under nitrogen atmosphere at 75°C. To synthesize the first batch of cores (C1), the vessel was filled with a monomer emulsion (ME0) of 18.0 g S, 2.00 g BDDA, 1.20 g SDS, and 1400 g deionized water. To synthesize the second batch of cores (C2),

ME0 contained 18.0 g S, 2.00 g BDDA, 1.08 g SDS, and 1400 g deionized water. While stirring at 250 rpm, both polymerizations were subsequently initiated with 0.360 g NaDS and 2.59 g NaPS. After a reaction time of 10 min, a monomer emulsion (ME1) was added continuously with a flow rate of 4.0 mL min^{-1}, using a rotary piston pump (Ismatec reglo-CPF digital, RH00). For the synthesis of C1, ME1 contained 410 g S, 41.0 g BDDA, 1.34 g SDS, 2.34 g KOH, 1.28 g Dowfax2A1, and 527 g deionized water. For the synthesis of C2, ME1 contained 513 g S, 51.3 g BDDA, 1.67 g SDS, 2.92 g KOH, 1.60 g Dowfax2A1, and 659 g deionized water. After complete addition of ME1, both reactions were kept at a constant temperature and stirred for an additional hour.

Interlayer-Shell-Synthesis: Two batches of core–shell–particles (CSP) were synthesized starting from above-described crosslinked core particles. The first batch (CSP1 based on C1) and second batch (CSP2 based on C2) only differ in composition of their cores C1 and C2, while the below-described synthesis of interlayer and shell followed the identical protocol. C1 and C2 were each diluted to a solid content of 8.00 wt%. 277 g of the diluted core particle-dispersion were filled in a 1 L double-wall reactor, equipped with a reflux condenser and a stirrer under nitrogen atmosphere at 75°C. While stirring at 250 rpm, the emulsion polymerization was subsequently initiated by adding 0.059 g NaDS and 0.342 g NaPS. After a reaction time of 15 min, a monomer emulsion (ME2) containing of 3.49 g MMA, 0.201 g ALMA, 0.067 g Dowfax2A1, 0.034 g SDS, and 14.9 g deionized water was continuously added with a constant flow rate of 1.0 mL min^{-1} using a rotary piston pump. After complete addition of ME2 and an additional 15 min, the emulsion polymerization was reinitiated by the addition of 0.040 g NaPS and continuously stirred for another 10 min. Afterward, a monomer emulsion (ME3) containing 43.8 g EA, 1.35 g HEMA, 0.178 g SDS, 0.143 g Dowfax2A1, 0.250 g KOH, and 59.0 g deionized water was continuously added with a flow rate of 1.0 mL min^{-1} using a rotary piston pump. After complete addition of ME3, the reaction mixture was kept at a constant temperature and stirred for an additional hour.

Processing: The lyophilized CSP were mixed with 0.03 wt% Carbon Black (Evonik Channel Type Black 4, particle size < 45 µm) and afterward extruded at 120°C and 100 rpm (Thermo Scientific HAAKE MiniLab 3 Micro-Compounder). SEM images of the untreated carbon black are provided in Figure S10 (Supporting Information), indicating that the sizes of carbon black particles range from 2 to 20 µm. The extruded mass was 3D-printed on a Saarpricom Delta UpSD 3D-Printer, equipped with a 0.4 mm Nozzle. 3D-Models were downloaded from cited sources or designed using Autodesk Meshmixer, Autodesk Inventor and Blender. Slicing was performed using Simplify3D V4.1.2. GCode- and STL-Files are available on request from the authors.

Analysis: Dynamic light scattering (DLS) measurements of the diluted particle dispersion after each polymerization step were performed on a Zetasizer ZS 90 by Malvern Instruments equipped with a 4 mW, 633 nm HeNe Laser. All measurements were carried out at 25°C at an angle of 90° with a five-fold determination of 15 runs. Automated data acquisition in 300 size classes and peak determination was carried out using Zetasizer Nano software. Intensities were normalized with respect to the highest value in each measurement.

For transmission electron microscopy (TEM) studies, a diluted polymer dispersion was drop-casted on a carbon-coated copper grid. The dispersion medium was allowed to evaporate at ambient conditions for 12 h. TEM experiments were carried out using a JEOL JEM-2100 electron microscope at a nominal acceleration voltage of 200 kV with a Gatan Orius SC100 CCD camera in bright field mode. For the determination of particle diameters, 20 particles per batch were analyzed using the software ImageJ. Scanning electron microscopy (SEM) of printed surfaces was carried out on a Zeiss Gemini500 Sigma VP device using the software SmartSEM Version 6.07, with accelerating voltages between 2 and 4 kV.

For evaluation of the thermal properties of the synthesized CSP, differential scanning calorimetry (DSC) was carried out with a Netzsch 214 F1 Polyma with a heating rate of 10 K min^{-1} and a sample mass of 5.0 mg. Glass transitions and oxidation inductions were determined using Netzsch Proteus software. Heat fluxes were normalized with

ADVANCED
SCIENCE NEWS

www.advancedsciencenews.com

ADVANCED
FUNCTIONAL
MATERIALS

www.afm-journal.de

respect to the heat flux at 60°C. Thermogravimetric analyses (TGA) were performed with a Netzsch TG 209 F1 Libra system with a heating rate of 10 K min⁻¹ and a sample mass of 15.0 mg. The onset of thermal degradation was determined using Netzsch Proteus software.

Temperature-dependent rheological properties were determined using an Anton Paar MCR501 oscillatory rheometer with a 25 mm plate-plate geometry, with a heating rate of 5 K min⁻¹. Complex dynamic viscosities were calculated with Anton Paar RheoCompass software. Shear rate-dependent rheological properties were determined using a Thermo Scientific HAAKE MiniLab 3 Micro-Compounder, equipped with a rectangular slit capillary at 140°C. Steady shear dynamic viscosities were calculated with PolySoft OS Software. Measurements were conducted at six different shear rates with a double determination for each shear rate. Shore-A hardness was determined using a Sauter HBA 100-0 Durometer.

Tensile tests were performed using an Instron 8513 universal testing machine, equipped with a 5 kN load cell, with a testing speed of 0.5 mm s⁻¹. Data was obtained using Labview 5.1.

Pictures of 3D-printed objects were taken with a Canon EOS 250 digital single lens reflex camera. Reflection spectra were recorded using an Ocean Optics fiber FLAME vis/NIR fiber spectrometer USB2000, combined with an Ocean Optics deuterium/tungsten halogen lamp DT mini 2. All spectra were recorded in reflection mode. Peak wavelengths were determined using OceanView software. Reflection intensities were normalized with respect to the highest value in each measurement series. For angle-dependent measurements, the spectrometer was operated in θ-2θ-mode. An angle of $\theta = 90°$ refers to normal incidence.

Statistical Analysis: Different types of standard deviations σ were calculated in this work. As they differ in the nature of the obtained data, calculations vary slightly. We used Equation 5 to calculate the standard deviation σ_{DLS} of the hydrodynamic particle diameters, obtained by means of DLS measurements. Therein $D_{DLS,i}$ represents a size class i with the normalized intensity I_i. The sample size N includes all size classes of a measurement ($N = 300$). The overall mean size D_{DLS} was calculated as weighted average.

$$\sigma_{DLS} = \sqrt{\frac{\sum_{i=1}^{i=N} I_i \cdot (D_{DLS,i} - D_{DLS})^2}{\sum_{i=1}^{i=N} I_i}} \tag{5}$$

We used Equation 6 to calculate the standard deviation σ_{TEM} of particle diameters in dried state, as determined by TEM-measurements. Therein n describes the sample size ($n = 20$) of a random sample survey and $D_{TEM,i}$ represents the TEM-diameter of an individual particle i. D_{TEM} was calculated as mean diameter of the 20 individual particles.

$$\sigma_{TEM} = \sqrt{\frac{\sum_{i=1}^{i=n} (D_{TEM,i} - D_{TEM})^2}{n-1}} \tag{6}$$

We used Equation 7 to calculate the standard deviation σ_λ of the measured reflected wavelengths λ(measured), compared to expected wavelengths λ(expected). Expected wavelengths were calculated as described in the main text, where they are labelled λ(Bragg), λ(Ruhl) and λ(Viel), respectively. The value of λ(expected)$_i$ depends on the angle of measurement and the applied strain and was therefore calculated for each individual measurement i of a test series. The sample size N includes all measurements i of a test series, representing a total statistical population.

$$\sigma_\lambda = \sqrt{\frac{\sum_{i=1}^{i=N} \left[\lambda(\text{measured})_i - \lambda(\text{expected})_i \right]^2}{N}} \tag{7}$$

Supporting Information

Supporting Information is available from the Wiley Online Library or from the author.

Conflict of Interest

The authors declare no conflict of interest.

Data Availability Statement

The data that support the findings of this study are available from the corresponding author upon reasonable request.

[1] J. Teyssier, S. V. Saenko, D. van der Marel, M. C. Milinkovitch, *Nat. Commun.* **2015**, *6*, 6368.

[2] K. Chung, S. Yu, C. J. Heo, J. W. Shim, S. M. Yang, M. G. Han, H. S. Lee, Y. Jin, S. Y. Lee, N. Park, J. H. Shin, *Adv. Mater.* **2012**, *24*, 2375.

[3] a) G. Isapour, M. Lattuada, *Adv. Mater.* **2018**, *30*, 1707069; b) M. Vatankhah-Varnosfaderani, A. N. Keith, Y. Cong, H. Liang, M. Rosenthal, M. Sztucki, C. Clair, S. Magonov, D. A. Ivanov, A. V. Dobrynin, S. S. Sheiko, *Science* **2018**, *359*, 1509; c) K. Chen, Q. Fu, S. Ye, J. Ge, *Adv. Funct. Mater.* **2017**, *27*, 1702825; d) C. G. Schäfer, M. Gallei, J. T. Zahn, J. Engelhardt, G. P. Hellmann, M. Rehahn, *Chem. Mater.* **2013**, *25*, 2309; e) P. Wu, J. Wang, L. Jiang, *Mater. Horiz.* **2020**, *7*, 338; f) D. Scheid, C. Lederle, S. Vowinkel, C. G. Schäfer, B. Stühn, M. Gallei, *J. Mater. Chem. C* **2014**, *2*, 2583; g) F. Liu, M. W. Urban, *Prog. Polym. Sci.* **2010**, *35*, 3.

[4] a) W. Wang, Y. Zhou, L. Yang, X. Yang, Y. Yao, Y. Meng, B. Tang, *Adv. Funct. Mater.* **2022**, *32*, 2204744; b) F. Bian, L. Sun, H. Chen, Y. Wang, L. Wang, L. Shang, Y. Zhao, *Adv. Sci.* **2022**.

[5] a) G. Isapour, M. Lattuada, *ACS Appl. Nano Mater.* **2021**, *4*, 3389; b) P. Wu, X. Shen, C. G. Schäfer, J. Pan, J. Guo, C. Wang, *Nanoscale* **2019**, *11*, 20015.

[6] a) A. Núñez-Montenegro, D. M. A. Crista, J. C. G. E. da Silva, *Eur. J. Wood. Wood. Prod.* **2020**, *78*, 293; b) L. Shang, W. Zhang, K. Xu, Y. Zhao, *Mater. Horiz.* **2019**, *6*, 945.

[7] a) Z. Cai, Z. Li, S. Ravaine, M. He, Y. Song, Y. Yin, H. Zheng, J. Teng, A. Zhang, *Chem. Soc. Rev.* **2021**, *50*, 5898; b) J. Ge, Y. Yin, *Angew. Chem., Int. Ed. Engl.* **2011**, *50*, 1492.

[8] a) Q. Zhao, C. E. Finlayson, D. R. Snoswell, A. Haines, C. G. Schäfer, P. Spahn, G. P. Hellmann, A. V. Petukhov, L. Herrmann, P. Burdet, P. A. Midgley, S. Butler, M. Mackley, Q. Guo, J. J. Baumberg, *Nat. Commun.* **2016**, *7*, 11661; b) T. Ruhl, P. Spahn, G. P. Hellmann,

Polymer **2003**, *44*, 7625; c) T. Winter, A. Boehm, V. Presser, M. Gallei, *Macromol. Rapid. Commun.* **2021**, *42*, 2000557; d) M. Bitsch, A. K. Boehm, A. Grandjean, G. Jung, M. Gallei, *Molecules* **2021**, *26*, 7350; e) C. S. Chern, *Prog. Polym. Sci.* **2006**, *31*, 443.

[9] a) M. Gallei, *Macromol. Rapid. Commun.* **2018**, *39*, 1700648; b) C. E. Finlayson, J. J. Baumberg, *Polym. Int.* **2013**, *62*, 1403.

[10] a) L. Gonzalez-Urbina, K. Baert, B. Kolaric, J. Perez-Moreno, K. Clays, *Chem. Rev.* **2012**, *112*, 2268; b) G. von Freymann, V. Kitaev, B. V. Lotsch, G. A. Ozin, *Chem. Soc. Rev.* **2013**, *42*, 2528.

[11] a) P. Spahn, C. E. Finlayson, W. M. Etah, D. R. E. Snoswell, J. J. Baumberg, G. P. Hellmann, *J. Mater. Chem.* **2011**, *21*, 8893; b) A. P. Hynninen, J. H. Thijssen, E. C. Vermolen, M. Dijkstra, A. van Blaaderen, *Nat. Mater.* **2007**, *6*, 202.

[12] M. Li, Q. Lyu, B. Peng, X. Chen, L. Zhang, J. Zhu, *Adv. Mater.* **2022**, *34*, 2110488.

[13] a) K. R. Phillips, G. T. England, S. Sunny, E. Shirman, T. Shirman, N. Vogel, J. Aizenberg, *Chem. Soc. Rev.* **2016**, *45*, 281; b) R. Xiong, J. Luan, S. Kang, C. Ye, S. Singamaneni, V. V. Tsukruk, *Chem. Soc. Rev.* **2020**, *49*, 983; c) P. Liu, L. Bai, J. Yang, H. Gu, Q. Zhong, Z. Xie, Z. Gu, *Nanoscale Adv.* **2019**, *1*, 1672.

[14] P. Jiang, G. N. Ostojic, R. Narat, D. M. Mittleman, V. L. Colvin, *Adv. Mater.* **2001**, *13*, 389.

[15] a) P. Jiang, M. J. McFarland, *J. Am. Chem. Soc.* **2004**, *126*, 13778; b) A. Mihi, M. Ocaña, H. Míguez, *Adv. Mater.* **2006**, *18*, 2244.

[16] a) O. L. J. Pursiainen, J. J. Baumberg, H. Winkler, B. Viel, P. Spahn, T. Ruhl, *Adv. Mater.* **2008**, *20*, 1484; b) C. G. Schäfer, T. Winter, S. Heidt, C. Dietz, T. Ding, J. J. Baumberg, M. Gallei, *J. Mater. Chem. C* **2015**, *3*, 2204.

[17] Q. Zhao, C. E. Finlayson, C. G. Schäfer, P. Spahn, M. Gallei, L. Herrmann, A. V. Petukhov, J. J. Baumberg, *Adv. Opt. Mater.* **2016**, *4*, 1494.

[18] G. Chen, W. Hong, *Adv. Opt. Mater.* **2020**, *8*, 2000984.

[19] a) S. A. M. Tofail, E. P. Koumoulos, A. Bandyopadhyay, S. Bose, L. O'Donoghue, C. Charitidis, *Mater. Today* **2018**, *21*, 22; b) X. Wang, M. Jiang, Z. Zhou, J. Gou, D. Hui, *Composites, Part B* **2017**, *110*, 442; c) M. Su, Y. Song, *Chem. Rev.* **2021**, 5144; d) B. Narupai, A. Nelson, *ACS Macro Lett.* **2020**, *9*, 627.

[20] Sculpteo, *The State of 3D Printing*, sculpteo.com, Paris **2021**.

[21] a) A. J. Boydston, B. Cao, A. Nelson, R. J. Ono, A. Saha, J. J. Schwartz, C. J. Thrasher, *J. Mater. Chem. A* **2018**, *6*, 20621; b) M. Nadgorny, A. Ameli, *ACS Appl. Mater. Interfaces* **2018**, *10*, 17489.

[22] Z. Jiang, B. Diggle, M. L. Tan, J. Viktorova, C. W. Bennett, L. A. Connal, *Adv. Sci.* **2020**, *7*, 2001379.

[23] a) D. K. Patel, B.-E. Cohen, L. Etgar, S. Magdassi, *Mater. Horiz.* **2018**, *5*, 708; b) X. Qian, X. Cai, M. Su, F. Li, W. Fang, Y. Li, X. Zhou, Q. Li, X. Feng, W. Li, X. Hu, X. Wang, C. Pan, Y. Song, *Adv. Mater.* **2018**, *30*, 1800291.

[24] B. Cao, N. Boechler, A. J. Boydston, *Polymer* **2018**, *152*, 4.

[25] a) R. C. Rohde, A. Basu, L. B. Okello, M. H. Barbee, Y. Zhang, O. D. Velev, A. Nelson, S. L. Craig, *Polym. Chem.* **2019**, *10*, 5985; b) G. I. Peterson, D. E. Pei, M. Yurtoglu, M. B. Larsen, S. L. Craig, M. A. Ganter, D. W. Storti, A. J. Boydston, *Rapid Prototyp. J.* **2015**, *21*, 520; c) G. I. Peterson, M. B. Larsen, M. A. Ganter, D. W. Storti, A. J. Boydston, *ACS Appl. Mater. Interfaces* **2015**, *7*, 577.

[26] a) F. Chen, Y. Huang, R. Li, S. Zhang, B. Wang, W. Zhang, X. Wu, Q. Jiang, F. Wang, R. Zhang, *Chem. Commun.* **2021**, *57*, 13448; b) Z. Xuan, J. Li, Q. Liu, F. Yi, S. Wang, W. Lu, *Innovation* **2021**, *2*, 100081.

[27] a) L. Li, Q. Lin, M. Tang, A. J. E. Duncan, C. Ke, *Chemistry* **2019**, *25*, 10768; b) B. B. Patel, D. J. Walsh, D. H. Kim, J. Kwok, B. Lee, D. Guironnet, Y. Diao, *Sci. Adv.* **2020**, *6*, eaaz7202.

[28] a) M. Nadgorny, Z. Xiao, C. Chen, L. A. Connal, *ACS Appl. Mater. Interfaces* **2016**, *8*, 28946; b) B. M. Boyle, T. A. French, R. M. Pearson, B. G. McCarthy, G. M. Miyake, *ACS Nano* **2017**, *11*, 3052.

[29] a) Y. Liu, H. Wang, J. Ho, R. C. Ng, R. J. H. Ng, V. H. Hall-Chen, E. H. H. Koay, Z. Dong, H. Liu, C. W. Qiu, J. R. Greer, J. K. W. Yang, *Nat. Commun.* **2019**, *10*, 4340; b) D. Han, Z. Lu, S. A. Chester, H. Lee, *Sci. Rep.* **2018**, *8*, 1963; c) Q. Zhou, J. G. Park, J. Bae, D. Ha, J. Park, K. Song, T. Kim, *Adv. Mater.* **2020**, *32*, 2001467; d) Z. Hu, N. P. Bradshaw, B. Vanthournout, C. Forman, K. Gnanasekaran, M. P. Thompson, P. Smeets, A. Dhinojwala, M. D. Shawkey, M. C. Hersam, N. C. Gianneschi, *Chem. Mat.* **2021**, *33*, 6433.

[30] C. G. Schäfer, *Ph.D. Thesis*, Technische Universität, Darmstadt, Germany **2016**.

[31] C. G. Schäfer, B. Viel, G. P. Hellmann, M. Rehahn, M. Gallei, *ACS Appl. Mater. Interfaces* **2013**, *5*, 10623.

[32] L. D. Bonifacio, B. V. Lotsch, D. P. Puzzo, F. Scotognella, G. A. Ozin, *Adv. Mater.* **2009**, *21*, 1641.

[33] L. A. Wood, *J. Polym. Sci.* **1958**, *28*, 319.

[34] J. Xu, B. Chen, Q. Zhang, B. Guo, *Polymer* **2004**, *45*, 8651.

[35] M. Dost, Elf Archer Bust, www.thingiverse.com/thing:2314063, remixed by L. Siegwardt, (accessed: November **2022**).

[36] O. L. J. Pursiainen, J. J. Baumberg, K. Ryan, J. Bauer, H. Winkler, B. Viel, T. Ruhl, *Appl. Phys. Lett.* **2005**, *87*, 101902.

[37] O. L. J. Pursiainen, J. J. Baumberg, H. Winkler, B. Viel, P. Spahn, T. Ruhl, *Opt. Express* **2007**, *15*, 9553.

[38] a) C. E. Finlayson, G. Rosetta, J. J. Baumberg, *Materials* **2021**, *14*, 5298; b) C. E. Finlayson, J. J. Baumberg, *Materials* **2017**, *10*, 688.

[39] J. Prusa, in *Basics of 3D Printing*, Prusa Research, Prague **2020**.

[40] H. S. Wong, M. Mackley, S. Butler, J. Baumberg, D. Snoswell, C. Finlayson, Q. Zhao, *J. Rheol.* **2014**, *58*, 397.

[41] a) C. E. Finlayson, C. Goddard, E. Papachristodoulou, D. R. Snoswell, A. Kontogeorgos, P. Spahn, G. P. Hellmann, O. Hess, J. J. Baumberg, *Opt. Express* **2011**, *19*, 3144; b) C. E. Finlayson, P. Spahn, D. R. Snoswell, G. Yates, A. Kontogeorgos, A. I. Haines, G. P. Hellmann, J. J. Baumberg, *Adv. Mater.* **2011**, *23*, 1540.

[42] K. R. Phillips, N. Vogel, Y. Hu, M. Kolle, C. C. Perry, J. Aizenberg, *Chem. Mater.* **2014**, *26*, 1622.

[43] S. Campbell, Ape Servant, www.thingiverse.com/thing:2768992, gorilla remix by L. Siegwardt, (accessed: November **2022**).

[44] S. Campbell, Ape Servant, www.thingiverse.com/thing:2768992, chimpanzee remix by L. Siegwardt, (accessed: November **2022**).

[45] a) A. Kontogeorgos, D. R. Snoswell, C. E. Finlayson, J. J. Baumberg, P. Spahn, G. P. Hellmann, *Phys. Rev. Lett.* **2010**, *105*, 233909; b) T. Ruhl, G. P. Hellmann, *Macromol. Chem. Phys.* **2001**, *202*, 3502; c) B. Viel, T. Ruhl, G. P. Hellmann, *Chem. Mater.* **2007**, *19*, 5673.

[46] Z. D. Jastrzebski, *Nature and Properties of Engineering Materials*, Wiley, NY **1959**.

[47] T. Ding, G. Cao, C. G. Schafer, Q. Zhao, M. Gallei, S. K. Smoukov, J. J. Baumberg, *ACS Appl. Mater. Interfaces* **2015**, *7*, 13497.